Ring current morphology from MMS observations

X. Tan[1], M. W. Dunlop[1,2], X. -C. Dong[3], Y. -Y. Yang[4], Y. -S. Du[1], C. Shen[5], C. T. Russell[6], W. -L. Liu[1].

[1]School of Space and Environment, Beihang University, Beijing, China. [2]RAL_Space, STFC, Oxfordshire, UK. [3]Yunnan University, Kunming, China. [4]National Institute of Natural Hazards, Ministry of Emergency Management of China, Beijing, China., [5]Harbin Institute of Technology, Shenzhen, China., [6]Department of Earth, Planetary and Space Sciences, UCLA, Los Angeles, CA, USA.

Corresponding author: Malcolm Dunlop (m.dunlop@rl.ac.uk)

Key Points:

- General trends of ring current morphology are revealed by statistical analysis of current density, directly calculated from multi-spacecraft analysis of MMS data.
- Banana-like currents (at both inner and outer L-shells) are directly observed, resulting in both day-night and dawn-dusk asymmetry.
- Although an inner asymmetric eastward current is confirmed, no westward dusk-side, storm-time, ring current enhancement is observed.

Abstract

We directly estimate the *in situ* current density of the Earth's ring current (RC) using the curlometer method and investigate its morphology using the small spatial separations and high accuracy of the Magnetospheric Multiscale mission (MMS). Through statistical analysis of data from September 2015 to the end of 2016, covering the region of 2-8 R_E (Earth radius, 6371 km), we reveal an almost complete near-equatorial (within $\pm 20°$) RC morphology in terms of radial distance and local time (MLT) which complements and extends that found from previous studies. We found no evidence of RC enhancement on the dusk-side during geomagnetic active periods, but details of local time (MLT) asymmetries in, and the boundary between, the inner (eastward) and outer (westward) currents are revealed. We propose that part of the asymmetry demonstrated here suggests that in addition to the overall persistence of the westward RC, two large banana-like currents are directly observed, one which could arise from a peak of plasma pressure near ~4.8 R_E on the noon side and the other from a valley of plasma pressure which could arise near ~4.8 R_E on the night side.

Plain Language Summary

Large scale current systems existing in space affect the magnetic field on the surface of Earth and the ring current has a dominant influence. Space weather drives large variations in these currents which disturb the surface magnetic fields. When the disturbance is violent, it is called a magnetic storm and may have a disastrous impact on satellite and ground systems. Using the high-precision magnetic field data of the four spacecraft in NASA's Magnetospheric Multiscale mission (MMS), by employing a multi-spacecraft analysis method, we calculate the distribution of local current density in space. Through statistical analysis of the current in the region, we study its morphology. We confirm the asymmetry of the ring current found in previous studies and suggest a new explanation for part of the asymmetry, i.e., that the generally westward ring current is superimposed on closed, banana-like currents.

1 Introduction

The Earth's ring current (RC) plays an important role in the inner magnetosphere as it has a dominant effect on the Earth's geomagnetic field. It is therefore very important to study its distribution to better understand the inner magnetospheric current system and its dynamics. The RC is primarily formed by charged particles with energies from ~ 1 keV to hundreds of keV, captured by the Earth's magnetic field, which have gyration and drift motion caused by magnetic gradients and curvature (Parker 1957). The RC typically lies between 2-8 R_E and previously has been found to be reasonably well ordered within ±30° latitude. During magnetic storms, ionospheric particles may inject into the RC, dominating its morphology and dynamics (Daglis et al. 1999).

Preceding work has shown a pronounced asymmetry and other effects through the analysis of a variety of observation data, often related to the effects of the RC in adjacent regions. For example, Le and Russell (1998) pointed out that residual magnetic field measurements from low-altitude polar orbiting spacecraft are potentially useful as monitors of RC strength when they cross the polar cap. Le et al. (2011) studied its asymmetry by analyzing the influence on the distribution of the residual normal components of the magnetic field at LEO (low Earth orbit). *In situ* magnetic data, covering many years and a number of earlier missions, was used by Le, Russell, and Takahashi (2004); Jorgensen (2004) estimated the RC distribution for different levels of geomagnetic activity. These studies, however, have generally used only single spacecraft to extract components of the current density, $\boldsymbol{J}$ (so that assumptions have to be made to obtain $\boldsymbol{J}$ from magnetic residuals) and

indeed discrepancies exist between the morphology implied from low altitudes (to which other influences may contribute, such as field-aligned currents, FACs) and that seen *in situ*. The phased multi-spacecraft arrays of Cluster and THEMIS allowed direct estimates of *in situ* current densities (or at least some components) to be made from the magnetic field measurements for the first time (Vallat, Dandouras, and Dunlop 2005; Zhang et al. 2011; Yang et al. 2016). Being different from indirect observation at low latitudes, these studies directly show the morphology and characteristics of the RC, although the effects of the level of geomagnetic activity, and the full extent of the radial form, were not fully resolved due to some limitations of these missions: Cluster is limited in radial coverage of the RC, while the three THEMIS spacecraft cannot obtain the complete, *in situ* current vector. In other work, Yue et al. (2018) focused on plasma composition and pressure in the equatorial plane. Based on observational data, Tsyganenko et al. (2021); Sitnov et al. (2020), Stephens et al. (2020), Stephens et al. (2016) and Sitnov et al. (2020) have shown the evolutionary process of the equatorial current for geomagnetically active cases, through the use of the global semi-empirical magnetic field modelling, historical data mining, and as inferred from multi-mission magnetometer data.

The four spacecraft of MMS, launched by NASA on March 12, 2015, has the primary aim to study the micro-physical process of magnetic reconnection, but does have magnetic field survey data suitable for analysis of the RC region. Each spacecraft is equipped with identical instruments, providing high-precision, high-time resolution, scientific data. Here, we use data from the fluxgate magnetometer (FGM), which can achieve a measurement accuracy of 0.1 nT with cadence up to 128 Hz (Russell et al. 2014). The data from MMS have been used to investigate the detailed structure of the magnetopause (e.g. Dong et al. 2018) and magnetotail current sheet (e.g. Chen et al. 2021).

The left panel of Figure 1 shows orbits of MMS from September 1, 2015 to January 31, 2017. MMS operated in a low-inclination, elliptical orbit (apogee 12 R_E, perigee 1.2 R_E), thereby well covering the RC region of interest (ROI) to us here. The right panel shows the configuration of the four-spacecraft array. The unprecedentedly small spatial separations of the spacecraft array (ranging between 7-60 km) and the relatively regular tetrahedral configuration remain over most of the orbit. Thus, MMS can provide a new perspective, at higher spatial resolution of the RC form and behavior to that of previous studies. We emphasize that the aim of this paper is to apply the magnetic field measurements to calculate the current density directly.

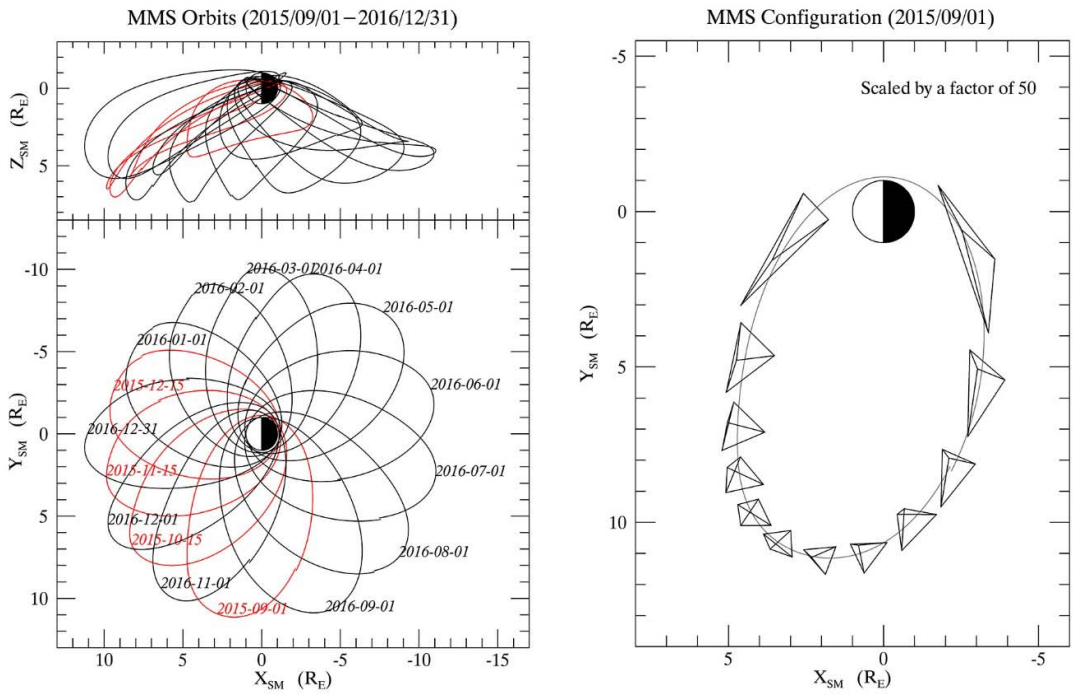

Figure 1. The left panel shows orbits of MMS from 1 September 2015 to 31 December 2016 in the SM coordinate system. The red curves indicate orbits in 2015, black curves indicate orbits in 2016. One single curve indicates orbit for one single day. Only one day's orbit is shown for each month to avoid making this plot too crowded. The latitude range shows that MMS mostly operated in the southern hemisphere of the magnetosphere during this time range, but completely spanned all MLTs. The right panel shows the orbit of MMS on 1 September 2015 and the configuration of its four-spacecraft array. The 12 tetrahedral shapes, with a 50-fold magnification, represent the constellations at every 2-hour time points, where the MMS array predominantly remained in a relatively regular tetrahedral configuration in the RC region.

2 Dataset and Methodology

The FGM instrument operated in survey mode for intervals when MMS was outside the science regions of interest (ROI), defined operationally for MMS. FGM survey data from September 1, 2015 to December 31, 2016 are used in this paper, with an accuracy of 0.1 nT and a time resolution of 16 Hz (inside the ROI) or 8 Hz (outside the ROI). We restrict the measurements to within ±20° of magnetic latitude. In addition, high resolution OMNI (HRO) one-minute accuracy interplanetary magnetic field (IMF) measurements, SYM_H, and AE indices data are used to classify the MMS data according to upstream solar wind conditions and geomagnetic activity, FGM data of Cluster from 2001 to 2019 are used for RC distribution results comparison.

We first average FGM survey data to one sample per minute in order to lower the magnetic field data frequency and filter out higher-frequency disturbances. Magnetic residuals are found by subtracting the International Geomagnetic Reference Field (IGRF-12) model (Thébault et al. 2015) from the measured magnetic field. Using residuals in the calculation reduces the presence of nonphysical (non-real) current signals generated by the neglect of strong, nonlinear gradients in the geomagnetic field (Dunlop et al. 2018).

The current density is calculated here using the curlometer method (Dunlop et al. 1988; Dunlop 2002; Dunlop et al. 2021), based on a linear expression of Ampere's law, for regions of high conductivity, so that the current density normal to a plane composed of any three spacecraft can be expressed as

$$\mu_0\langle \boldsymbol{J}\rangle \cdot \left(\Delta \boldsymbol{R}_i \times \Delta \boldsymbol{R}_j\right) = \Delta \boldsymbol{B}_i \cdot \Delta \boldsymbol{R}_j - \Delta \boldsymbol{B}_j \cdot \Delta \boldsymbol{R}_i \quad (1)$$

In this integral form, the vector $\boldsymbol{J}$ can thus be obtained, selectively component by component, from an array of four spacecraft (see other formalisms based on the barycenter of the spacecraft configurations, in Paschmann and Schwartz (1998)).

In fact, we can also get the current vector $\boldsymbol{J}$ from the plasma pressure (equation 2) (Daglis et al. 1999) and the plasma moments (equation 3):

$$\boldsymbol{J} = \frac{\boldsymbol{B}}{B^2} \times \left(\boldsymbol{\nabla} P_\perp + \frac{P_\parallel - P_\perp}{B^2}(\boldsymbol{B}\cdot\boldsymbol{\nabla})\boldsymbol{B}\right) \quad (2)$$

$$\boldsymbol{J} = q(n_i \boldsymbol{v}_i - n_e \boldsymbol{v}_e) \quad (3)$$

Each method has its own limitations and on the small MMS separation scales, results can match very closely in some cases, particularly for the calculation of $\boldsymbol{J}$ from either the plasma moments or the curlometer. The sampling of the ring current regions by MMS generally lies outside the ROI so that usually no fast plasma data is available. For a few events (which overlap with intervals within the operational ROI), however, MMS does provide fast plasma data. Figure 2 shows a comparison for a case study on 18 February 2016, when the FPI instrument was taking data. The electric current densities calculated by the three different methods are shown in this figure for the same time range and same scale. The curlometer result and the plasma current from the plasma moment (averaged over the spacecraft) are almost the same, suggesting that the current densities obtained from both methods are likely to be correct. The current density obtained from the pressure terms, however, shows key deviations, indicating that the assumptions for equation 2 are not always correct. Although the fast plasma data is not available for a full survey, we therefore believe that results obtained here by the curlometer method are credible, within the statistical conditions we have applied, giving confidence that the curlometer give a good representation of the current densities.

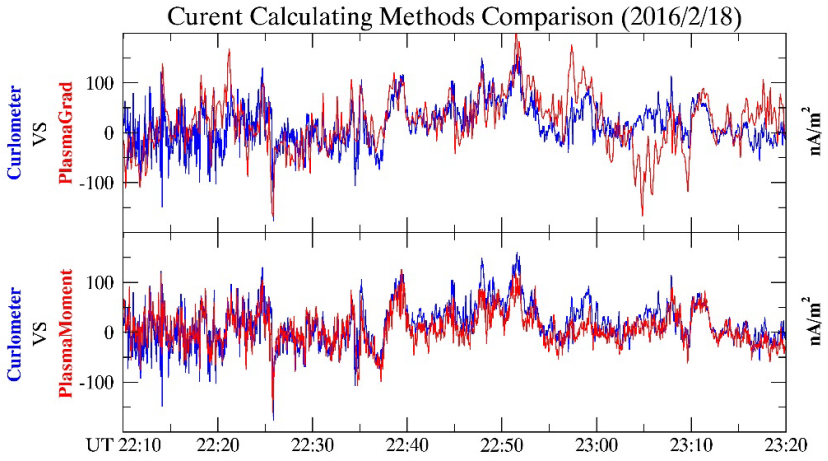

Figure 2. These two panels show magnitudes of current azimuthal components, calculated based on

MMS burst mode data from 23:22:10 to 23:23:20UT on 18 January 2016 by three methods: where the lower panel compares the curlometer vs plasma moments and the upper panel compares the curlometer vs pressure gradient. We used magnetic field measurements from the FGM instrument for the curlometer calculation, ion and electron number density and temperature measurements from the FPI instrument for the pressure gradient calculation and ion and electron number density and bulk velocity measurements from the FPI instrument for the plasma moment calculation. The average values of the four spacecraft ion/electron pressures and the average values of the four spacecraft plasma moments were used in estimating the currents in each calculation, as shown in this figure. The comparison illustrates that generally results from three different methods have the same order of magnitudes and same broad trends, but with key differences in the case of the pressure gradient calculation. Results from the curlometer and plasma moments are almost the same.

The results are presented here in the SM coordinate system (Earth centered, with the Z-axis along the dipole axis, the Y-axis perpendicular to both the dipole axis and the Sun–Earth line) and the X-axis from the right-hand rule (Russell 1971). We also expressed the vector current, $\boldsymbol{J}$, in components parallel ($\mathbf{J}_{/\!/}$) and perpendicular to the magnetic field (as the azimuthal ($J_{\perp(\varphi)}$) and radial($J_{\perp(r)}$) components) , where we mainly utilize the $J_{\perp(\varphi)}$ component. In the case study, it is shown that $J_{\varphi(sm)}$ is almost the same as $J_{\perp(\varphi)}$ in the region we study here because the magnetic field tends to be perpendicular to the SM equatorial plane. Many previous RC studies have directly analyzed J_{φ} instead (Yang et al. 2016; Zhang et al. 2011; Shen et al. 2014). The irregularity of the tetrahedral spacecraft configuration (which affects the quality of the calculation) can be indicated by "elongation" E = 1-(b/a) and "planarity" P = 1-(c/b) parameters, defined in terms of the eigenvalues of the corresponding volumetric tensor (where a, b and c represent, respectively, the square roots of the eigenvectors for the maximum, intermediate and minimum eigenvalues (Robert et al. 1998)). The linearized value of div$\mathbf{B}$ can also be obtained (Dunlop et al. 1988) and often is used to define a quality parameter Q = div$\mathbf{B}$/curl$\mathbf{B}$, which (indirectly) can also indicate the effect of nonlinear gradients, particularly if the tetrahedral configuration is regular. Considering the small spacing configuration of the MMS, it is good at capturing the detailed structure of the current. Within the focus range of this paper, the use of Q may cause the abandonment of some real current detail structures with small current densities, thus making the current density obtained by statistics too large. Therefore, we did not use this indicator to filter data in the statistical process.

We analyzed all the current density results obtained in the 2-8 R_E region to investigate the underlying mesoscale morphology. Additional, large intensity, small-scale current structures and ultra-low frequency (ULF) fluctuations in a percentage of passes, were also present (not shown in this paper). We are still studying these phenomena and concentrate the present work on describing the medium-scale trends in current structure. The ULF signatures make the current density fluctuate strongly, while the small scale currents have a small effect on the average current densities used to access the larger scale currents. To reduce the impact of the presence of fluctuations, results for a specific date are manually excluded (about 75% data remain, as listed in Table 1). In the statistical analysis, to eliminate possible abnormal data caused by extremely irregular tetrahedron configurations or positions deviating too far from the equatorial plane, we remove results that meet one of two conditions: 1. E > 0.85 or P > 0.85; and 2. |latitude| > 20°. The remaining data set is considered to provide stable (valid) $\boldsymbol{J}$ values.

Table 1. The selected data distribution in terms of date, with day of the month along the top header.

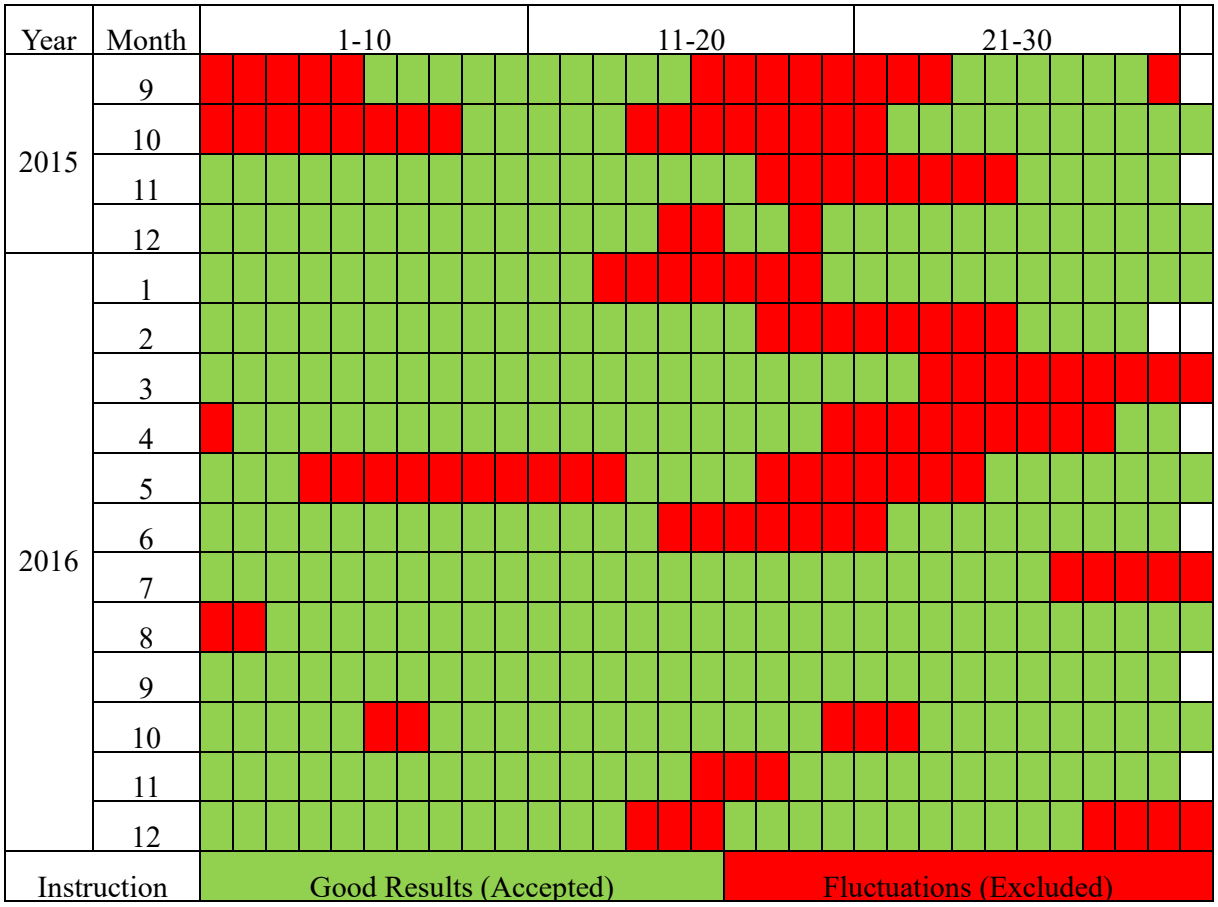

In order to explore the morphology statistically, we map spacecraft positions to the equatorial plane along the magnetic line of the IGRF field (omitting this step makes only a very small difference to the radial and MLT positions) and then we statistically bin $J_{\perp(\varphi)}$ into grids of (typically) 0.5 R_E × 1 hour of MLT, taking the median values (to exclude large outliers) of all valid $J_{\perp(\varphi)}$ at the bin centers (the variation of values within each bin define the error bars in the analysis below).When performing the mapping, we multiply the *in situ* current density by the coefficient $1/cos^3\lambda$ to correct from its off-equator values (where λ is the angle of the observation positions to the SM equatorial plane). The derivation of this coefficient is based on an ideal situation of a dipole magnetic field and isotropic assumption for the pressure, as follows:

$$\boldsymbol{j} = \boldsymbol{j_\nabla} + \boldsymbol{j_c} + \boldsymbol{j_G} = \frac{\boldsymbol{B}}{B^2} \times \left(\boldsymbol{\nabla} P_\perp + \frac{P_\parallel - P_\perp}{B^2} (\boldsymbol{B} \cdot \boldsymbol{\nabla}) \boldsymbol{B} \right) = \frac{\boldsymbol{B}}{B^2} \times \boldsymbol{\nabla} P$$

$$r = L cos^2 \lambda$$

$$B = \frac{M(1 + 3sin^2\lambda)^{1/2}}{r^3}$$

Assuming $P = f(L)$, then

$$\boldsymbol{\nabla} P = \frac{\partial f}{\partial L} \left(\frac{\partial L}{\partial r}, \frac{1}{r} \frac{\partial L}{\partial \lambda} \right) = \frac{\partial f}{\partial L} \left(\frac{1}{cos^2\lambda}, \frac{2sin\lambda}{cos^3\lambda} \right)$$

The direction of $\boldsymbol{\nabla} P$ is always perpendicular to B, so

$$|\boldsymbol{j}| = \left|\frac{\boldsymbol{B}}{B^2} \times \boldsymbol{\nabla} P\right| = \frac{|\boldsymbol{\nabla} P|}{B} = \frac{\frac{(1+3sin^2\lambda)^{1/2}}{cos^3\lambda}\frac{\partial f}{\partial L}}{\frac{M(1+3sin^2\lambda)^{1/2}}{r^3}} = \frac{L^3 cos^3\lambda}{M}\frac{\partial f}{\partial L}$$

$$\left|\frac{\boldsymbol{j_{eq}}}{\boldsymbol{j_{local}}}\right| = \frac{1}{cos^3\lambda} \quad (\mathbf{4})$$

We stress, however, that we are not seeking the strict equatorial distribution, but rather the average morphology within a low latitude range (following (Zhang et al. 2011) and (Vallat, Dandouras, and Dunlop 2005)).

3 Results

3.1 Case results

To illustrate the analysis we apply, we consider one case study, shown in Figure 3, for the pass 2015-09-22/05:00 to 05:50UT, where MMS moved from ~6.3 to ~8 R_E, during ~13:30 to 14:00MLT. Here, $\mathbf{J}_{\perp(\varphi)}$ remained westward, with a magnitude < 2 nA/m^2 and decreased slowly to zero, turning eastward at ~8.2 R_E. The radial component $\mathbf{J}_{\perp(\mathbf{r})}$ fluctuates but remains around zero on average. This case indicates that during this magnetically quiet period and for the outer region of the RC, the current remains westward, with a decreasing magnitude with distance. This broad form in fact is suggestive of the results in Figure 6 of (Tsyganenko et al. 2021). In that paper the dynamical structure of magnetosphere is reconstructed and the evolution of magnetospheric current system during substorms is modelled and the results here are consistent with the model in terms of the magnitude, direction and the time evolution of the RC. We don't reproduce the quantitatively model comparison in detail here, but the trends in (Tsyganenko et al. 2021) can be shown to be consistent with Figure 3. That is, at ~14:00MLT the RC magnitude falls from ~ 2nA/m^2 at ~6 R_E to zero at ~8 R_E in the westward direction and then revers to eastward. The favourable comparison to this case study suggests that the calculation results in this paper can be reliable.

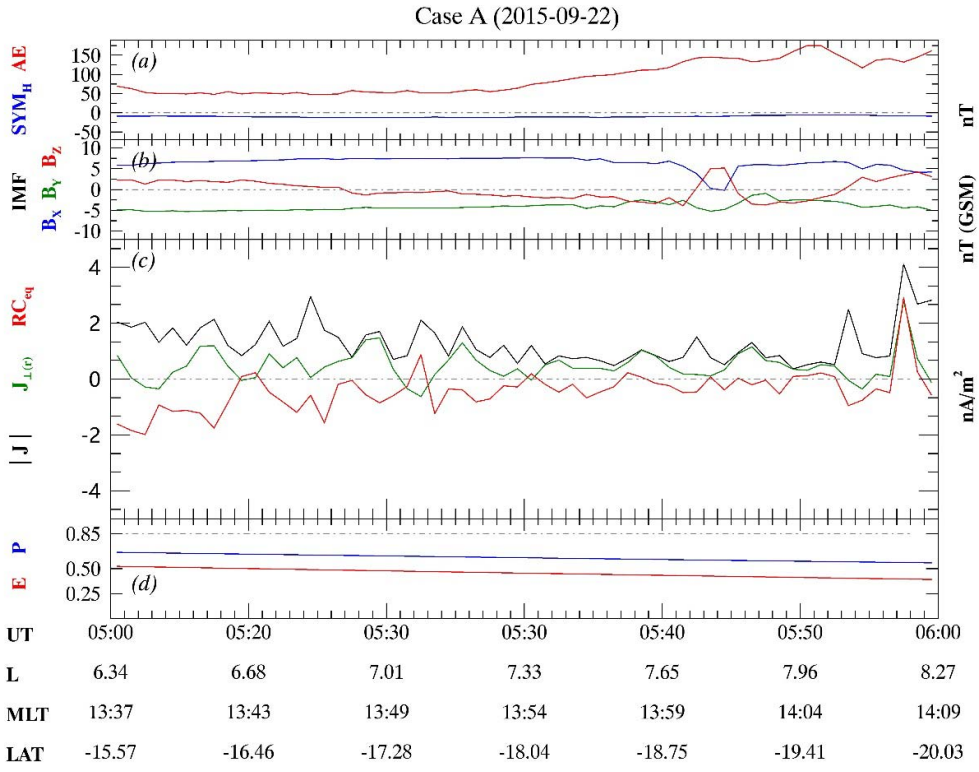

Figure 3. (a) SYM_H, AE index (b) IMF (c) Curlometer **J** in radial perpendicular component and total current density |**J**| (green and black), respectively. The red line represents the RC on the equatorial plane (multiplying the azimuthal perpendicular component of curlometer **J** by the λ coefficients). (d) E and P factors. The labelling on the bottom shows: UT, L-shell values, magnetic local time (MLT) and latitude (LAT).

We also choose a typical RC crossing event from 00:00-07:00 UT on September 13, 2015 to illustrate some key features of the RC, as shown in Figure 4, which shows an inner pass of MMS either side of perigee. The spacecraft fly inbound through the RC until 01:50 UT, during an interval when the IMF is initially relatively stable and then shows B_Z reversals, while the AE and SYM_H indices were stable with low (quiet) activity values. Between 01:50-04:20 UT, the tetrahedral configuration became irregular, resulting in nonphysical current density values (at other times $\mathbf{J}_{/\!/}$ remains small compared to $\mathbf{J}_{\perp}$). Subsequently, the spacecraft are outbound from 04:20-06:50 UT, when a dominant $\mathbf{J}_{\perp(\varphi)}$ was captured (with small values of $\mathbf{J}_{/\!/}$ and $\mathbf{J}_{\perp(r)}$) and a clear reversal of $\mathbf{J}_{\perp(\varphi)}$ identifies the boundary between the inner eastward and outer westward RC. The peak of $|\boldsymbol{J}| \sim 10$ nA/m^2, while the current reversal occurs at ~3.5 R_E. Conversely, during the inbound interval 00:20-01:50 UT, only a weak westward current was captured with $|\boldsymbol{J}| < 5$ nA/m^2. These two RC traversals, inbound and outbound, are highlighted by the cyan shaded regions. While differing RC values could potentially result from the initially southward IMF reversals, there is no dramatic change in geomagnetic activity, so that it is more likely due to the different local times and L-shells of the inbound and outbound passes, where the inbound pass covers radial distances above 5 R_E and predominantly around the dusk side, while the outbound pass covers radial distances from ~3 R_E, predominantly around midnight. This illustrates the evidence of local time (day-night) asymmetry of the RC as well as its radial profile which we explore statistically below. It is hard to distinguish the magenta curve, which presents the equatorial plane current (obtained from the local current

density (red), and scaled by the λ coefficient), demonstrating this correction makes little difference. The black curve, which presents $\mathbf{J}_{\varphi}$, is not visible as it is completely overlapped by the red curve, indicating $\mathbf{J}_{\varphi}$ is almost the same as $\mathbf{J}_{\perp(\varphi)}$ here. Indeed the radial and parallel components remain very small during the whole pass.

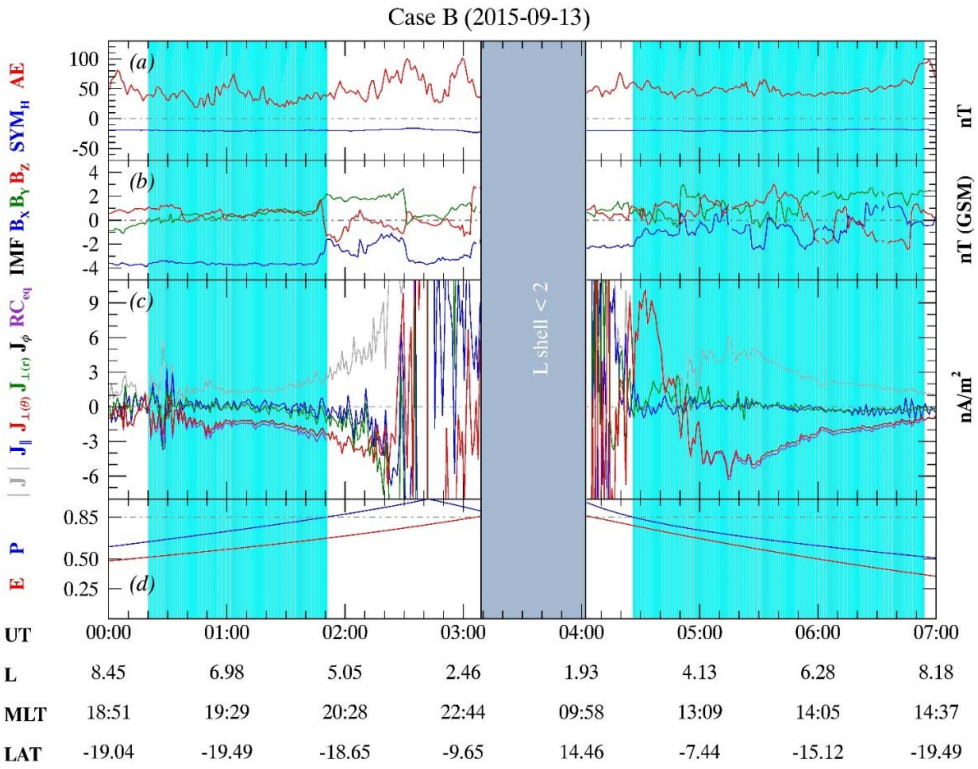

Figure 4. Panels are defined as for Figure 3 (but adding the full J components). The time interval is when MMS was within L_shell ≤ 8 and panels (a)-(d) have been masked when MMS was below L_shell = 2. The cyan shaded regions represent valid data points for the subsequent statistical process. There are total 239 valid points in this case.

3.2 Statistical results

Figure 5 shows the effective equatorial coverage of the orbits for valid (stable) data points, used between 2-8 R_E for a year of data from 2015-09-01 to 2016-12-30, in the XY_{SM} plane. The distributions of the binned, mean of $\mathbf{J}_{\perp(\varphi)}$ are then shown in Figure 6. Although the results do not cover all the regions evenly (there is low data coverage at some MLT and for some L values, where the criteria for a data gap is: orbit number ≤ 1 or data number < 10), Figure 6 does show the basic characteristics of the RC morphology. The three panels in Figure 6 highlight the mesoscale trends, showing the obvious day-night and dawn-dusk asymmetry, which is sensitive to L-shell (radial distance), and clear regions of eastward current. During storm time periods, this overall form doesn't change significantly, although the current density intensities and the radial boundaries do change. This mesoscale distribution is discussed in the sections below in terms of the averaged trends seen in MLT and L-shell (radial distance), referring back to Figure 6 when relevant. We do point out briefly here that the main distribution shows a broad region of westward current covering much of the region from noon-dawn, changing only in the pre-midnight sector. This broad

distribution recovers again post-midnight, but the dusk side region from noon shows a strong inner eastward current corresponding to a strong outer westward current in the same range of MLT.

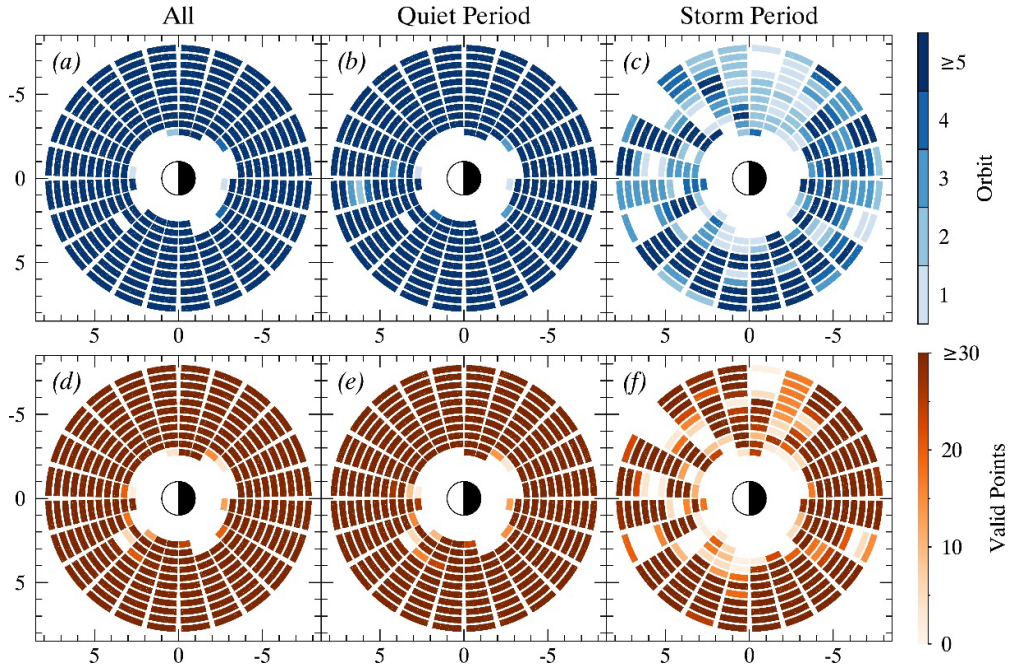

Figure 5. The orbits and valid points number distribution in the SM equatorial plane, following removal of abnormal values, in every 0.5 R_E × 1 hour (15° MLT) bin: (a) Number of orbits corresponding to valid data points (b) Number of orbits during non-storm time (c) Number of orbits during storm time (d) Number of valid data points (e) Number of points during non-storm time (f) Number of points during storm time.

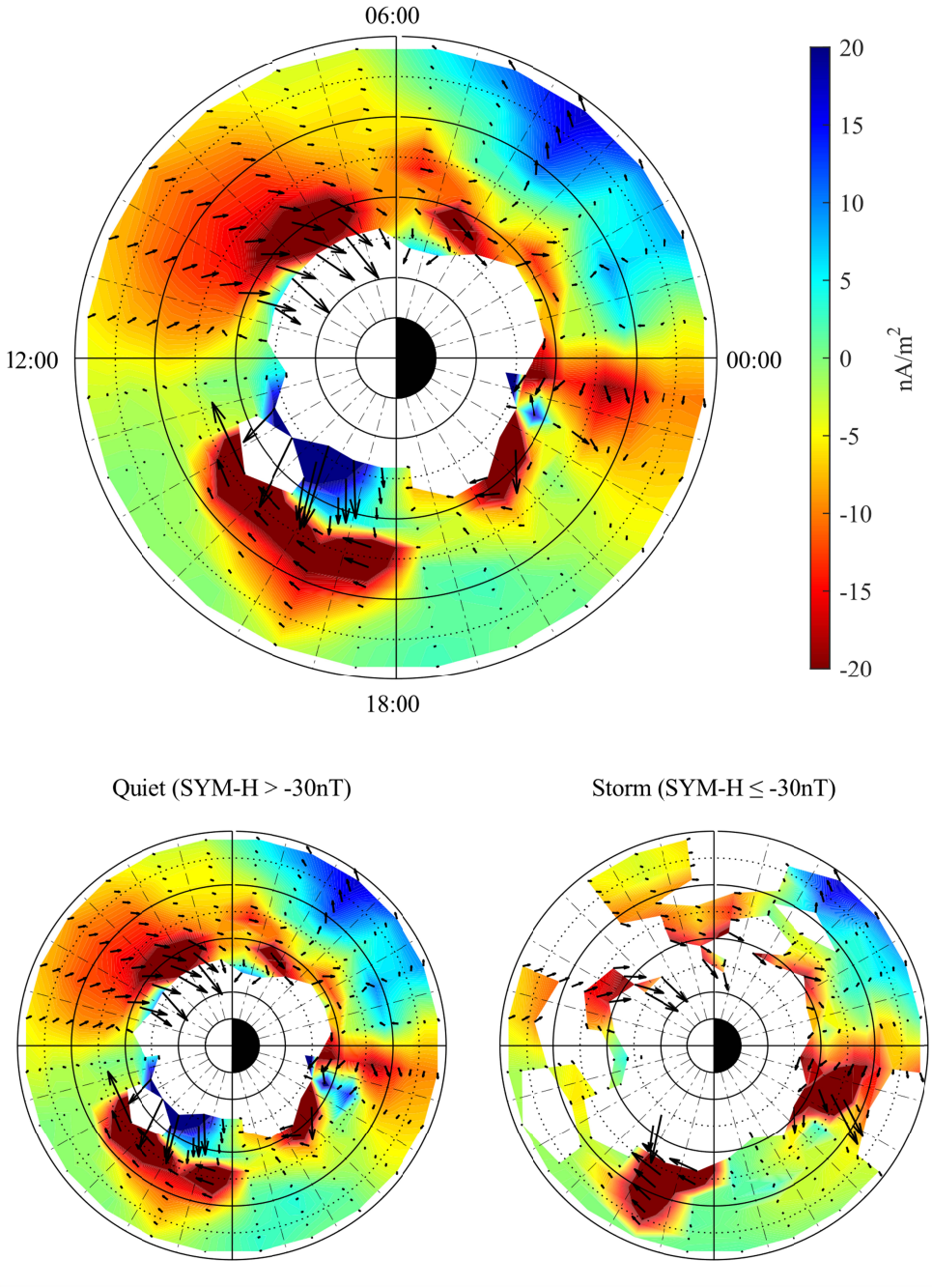

Figure 6. Colour contours of the $\mathbf{J}_{\perp(\varphi)}$ distribution for mean binned values under all magnetic conditions (upper panel) and during non-storm/storm periods (lower panels) for the SM equatorial plane. The magnetic local times are indicated with the radial grid at half hour intervals. The L-shells correspond to the radial distances, drawn as grid circles at 1 R_E intervals. Bins for which there is only one single orbit or fewer than 10 valid points are excluded. Positive current density values indicate eastward currents, while negative values correspond to westward currents. The arrows indicate the direction of the mean of $\mathbf{J}_{\perp}$ in each bin.

3.3 Mesoscale trends

These distributions may depend somewhat on the average prevailing conditions during the MMS coverage, so that it is also instructive to study the larger scale morphology trends of the RC in terms of the radial profiles (averaged over particular MLT) and MLT trends (for fixed ranges of radial distance) separately. In fact, we have made a preliminary study of Cluster data selected from the 19 years of data (from 2001 to 2019) to check the overall context of the MMS epoch used here and show these results later in Figure 11. We note here that for Cluster data from 2015-16, corresponding to the MMS period, the RC densities show similar ordering to MMS (as in Figure 5 above), and the current density intensities broadly agree although slightly lower than MMS as would be expected from the larger separation scales of the Cluster configurations (Dunlop, 2021). Below, we therefore probe the morphology trends by averaging the binned median values over different ranges of MLT to obtain the trends of $\mathbf{J}_{\perp(\varphi)}$ as a function of L-shell (statistically) and, conversely, averaging the median values over different ranges of L to obtain trends of $\mathbf{J}_{\perp(\varphi)}$ as a function of MLT.

We can analyze the trends for non-storm time (SYM_H > -30 nT) and storm-time (SYM_H ≤ -30 nT) geomagnetic activity separately, considering a range of different segments to reveal the tends in Figure 7. Figure 7(a) shows the relationship between $\mathbf{J}_{\perp(\varphi)}$ and L over all MLTs. The error bars represent the statistical variance (median absolute deviation), but there is a clear trend identifying the expected reversal between an outer westward current and an inner eastward current. During magnetically quiet times, $\mathbf{J}_{\perp(\varphi)}$ is eastward (~10 nA/m^2) within L~3.5 R_E, and westward at larger L; placing the average eastward-westward boundary at ~3.5 R_E. Between 3.5-5.5 R_E, the westward $\mathbf{J}_{\perp(\varphi)}$ peaks at ~ -12 nA/m^2. From 3.5-5.5 R_E, $\mathbf{J}_{\perp(\varphi)}$ remains westward, increasing and then decreasing in magnitude gradually. During magnetic storm periods this profile is broadly echoed, with enhanced $|\boldsymbol{J}|$ and there is strong evidence that $\mathbf{J}_{\perp(\varphi)}$ turns eastward (switching from -3 nA/m^2 to 5 nA/m^2) at ~3.2 R_E (as discussed further below, however, this boundary is dependent on MLT). The inner eastward $\mathbf{J}_{\perp(\varphi)}$ is suppressed, peaking at ~10 nA/m^2. Between 3.2-7.5 R_E, the westward $\mathbf{J}_{\perp(\varphi)}$ is enhanced. The peak position remains at ~4.0 R_E where $\mathbf{J}_{\perp(\varphi)}$ increases to ~13 nA/m^2 and then decreases slowly. We probe these variations more deeply by separating the distribution into MLT sectors below.

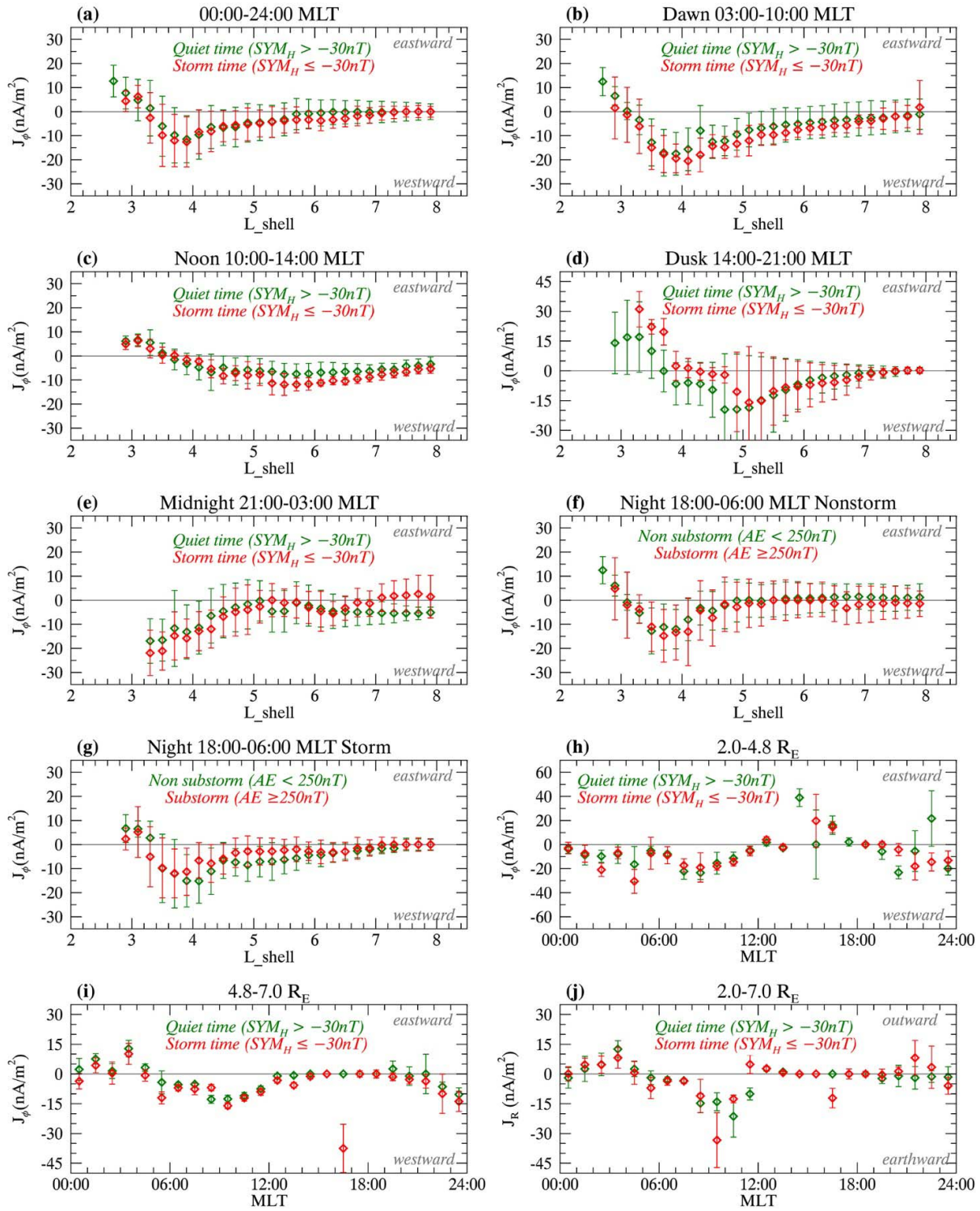

Figure 7. The upper seven panels show the relationship between $\mathbf{J}_{\perp(\varphi)}$ and L (a) for all MLTs, (b) on the dawn side (03:00-10:00 MLT), (c) on the noon side (10:00-14:00 MLT), (d) on the dusk side (14:00-21:00 MLT), (e) on the midnight side (21:00-03:00 MLT), (f) on the night side (18:00-00:00 MLT) during magnetically quiet periods, and (g) during storm time periods. The (h), (i) panels show the relationship between $\mathbf{J}_{\perp(\varphi)}$ and MLT in the range of (h) 2-4.8 R_E and (i) 4.8-7 R_E. The (j) panel shows the relationship between $\mathbf{J}_{\perp(R)}$ and MLT in the range of 2-7 R_E. According to the statistics of

L values every 0.2 R_E (a-g) or MLT every hour (h-j), the diamond square shows the median of **J**, the error bar shows the median absolutely deviation, the green is the statistical results of SYM_H > -30 nT (a-e, h, i, j) or AE < 250 nT (f, g), the red is the statistical result of SYM_H ≤ -30 nT (a-e, h, i, j) or AE ≥ 250 nT (f, g). A positive value of **J** corresponds to an eastward/outward current (negative value for westward/earthward current).

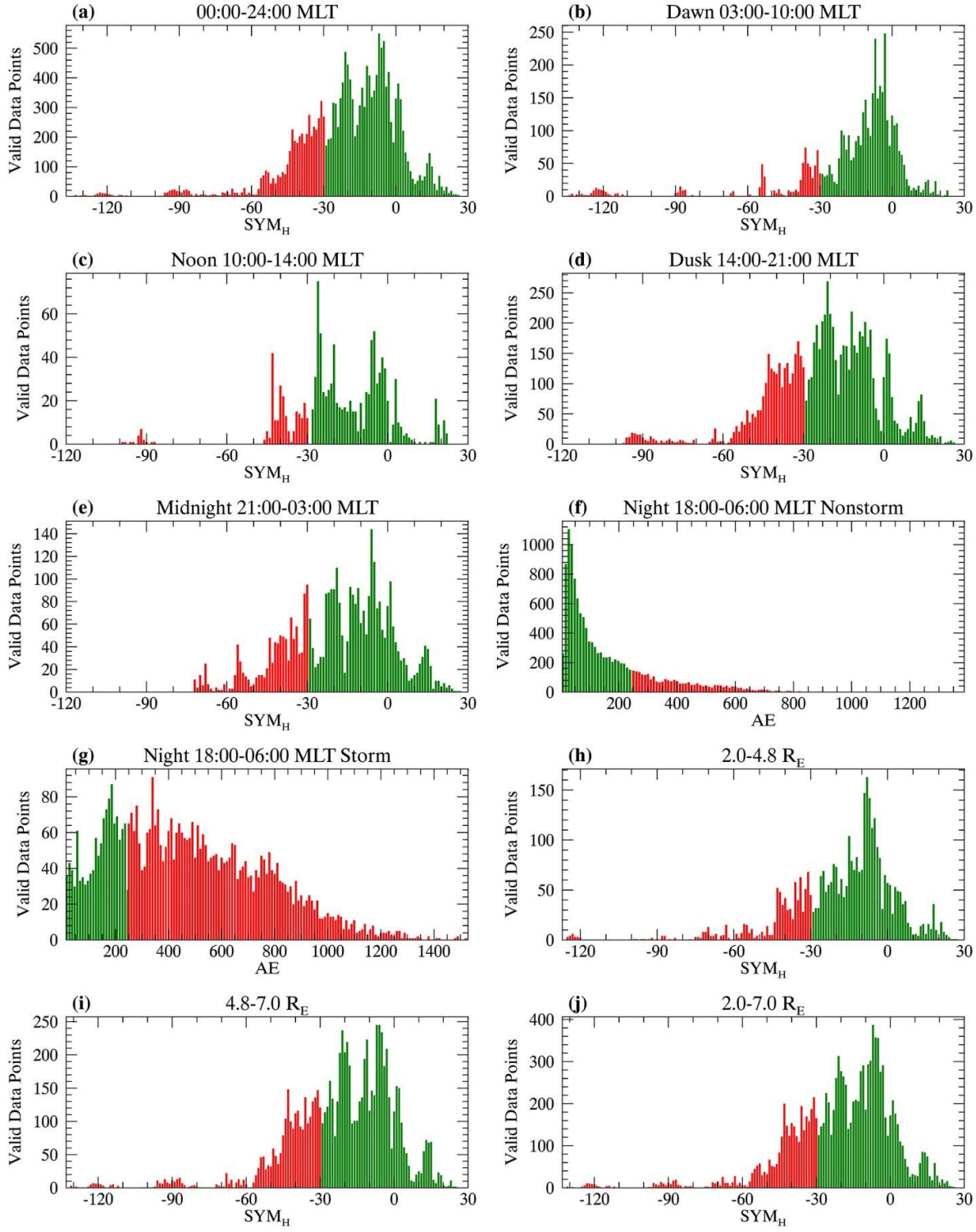

Figure 8. The distribution of valid data points for each panel of Figure 7.

In order to investigate the statistical dependence on MLT, we divide local time into four broad sectors: dawn, noon, dusk and midnight, and calculate the median of $\mathbf{J}_{\perp(\varphi)}$ over each MLT range. The four panels (b-e) of Figure 7 show the statistical results for $\mathbf{J}_{\perp(\varphi)}$ in each sector, where for dawn and dusk we extend the LT range to 7 hours. The dawn sector (03:00-10:00 MLT) trend is closest to that for all MLT and shows less variance from the error bars: $\mathbf{J}_{\perp(\varphi)}$ is westward, with a peak value of about -20 nA/m^2 between 3-7.5 R_E. Storm time conditions again increase $\mathbf{J}_{\perp(\varphi)}$ overall. Between 4.0-7.0 R_E, the impact of geomagnetic activity on $\mathbf{J}_{\perp(\varphi)}$ is significant; extending the region of enhanced current. Below ~3.0 R_E the effective eastward $\mathbf{J}_{\perp(\varphi)}$ boundary again occurs at lower L-shells than for quiet times. This enhanced (stronger) westward current on the dawn-side shows some consistency with (Zhang et al. 2011), whose results (under non-storm conditions) had a limited radial range of 4-4.5 R_E. The results here demonstrate that this dawn-side westward current (magnitude peak at ~27 nA/m^2) is more than two times stronger than average westward current peak for all MLTs. The eastward-westward current boundary is consistent with (Shen et al. 2014) and (Yang et al. 2016), who also noted the behaviour of the position of this boundary and found a similar radial profile (for all MLT) at distances up to 7-8 R_E.

The extended dusk sector (14:00-21:00 MLT) shows a dominant eastward current on the dusk-side, where the reversal boundary is located at larger L-shell: $\mathbf{J}_{\perp(\varphi)}$ is eastward below ~3.7 R_E during quiet times, where its magnitude increases to a maximum of ~15 nA/m^2 at L ~3.3 R_E. A westward $\mathbf{J}_{\perp(\varphi)}$ exists in the range 3.7-7.5 R_E with a peak value of ~ 20nA/m^2 at L~5 R_E. During magnetic storm periods, the boundary moves outward to ~4.2 R_E and the eastward current increases to a maximum of ~10 nA/m^2 in the range 6-7 R_E and decreases in the range 4.2-5 R_E. We note, however, that, referring back to Figure 6, we see the strong competing effects between the eastward/westward currents both in radial distance (L-shell) and MLT. This may have the result that the overall westward current is suppressed by the MLT averaging. Plotting the mean values rather than the median values for panel (d) in Figure 7 reveal the eastward to westward reversal with L-shell more clearly.

We therefore interpret this asymmetry in the dawn-dusk trends as broadly showing the presence of an enhanced dawn-side, westward current (between 3-7.5 R_E), which is suppressed on the dusk-side by the two competing effects of an eastward partial RC (between 3-4.0 R_E) and a weaker westward current. The distributions in Figure 6 also show that the eastward current is dominant in the post-noon sector, as compared to the pre-midnight sector. Nevertheless, the enhancement of the partial RC is not clearly seen in the current densities during storm conditions. This may be due to both the strengthening of the eastward current, moving to larger L-shells, and the widening of the region containing the westward current (so that the local current densities do not show a clear increase, but the total current does increase). Storm conditions suppress inner eastward current and enhance outer westward current on the dawn-side, but enhance the inner eastward current, suppressing the westward current in a small L range and slightly enhancing the westward current in a larger L range on the dusk-side.

The extended dawn/dusk MLT range we use reduces the noon-side range to 10:00-14:00 MLT. We again see evidence that the eastward-westward boundary lies at higher L-shells than on the dawn side: within 3.5 R_E, $\mathbf{J}_{\perp(\varphi)}$ is wholly eastward, while beyond 3.5 R_E, $\mathbf{J}_{\perp(\varphi)}$ is initially westward, dipping at ~4.6 R_E, before becoming more strongly westward and then falling off with L-shell (this echoes the behaviour of the overall trend for all MLT). During magnetically quiet periods, the eastward $\mathbf{J}_{\perp(\varphi)}$ increases to a maximum value of ~8 nA/m^2. During magnetic storms, $|\mathbf{J}_{\perp(\varphi)}|$

decreases significantly in the eastward direction and increases in the westward direction; the most obvious enhancement is just after 4.5 R_E.

The midnight sector (21:00-03:00 MLT) shows a dominant westward current, increasing in magnitude with lower L-shell values (although there are no statistical points below ~3.2 R_E). During quiet times, within 4.8 R_E, $\mathbf{J}_{\perp(\varphi)}$ grows more rapidly to a maximum value of ~17 nA/m^2; although we note that below ~3.8 R_E the error bars (linked to fluctuations in $\mathbf{J}_{\perp(\varphi)}$, pass by pass) become large. In the range 4.2-8 R_E, the median of $\mathbf{J}_{\perp(\varphi)}$ for quiet time is eastward with a current density of ~5 nA/m^2. During storm periods, the range of westward $\mathbf{J}_{\perp(\varphi)}$ condenses to around 6.5 R_E. The current density magnitude of the westward $\mathbf{J}_{\perp(\varphi)}$ in the range below ~5 R_E is slightly enhanced.

The influence of substorm activity (flagged by an AE threshold of 250 nT) on the distribution of $\mathbf{J}_{\perp(\varphi)}$ with L on the night side hemisphere (18:00-06:00 MLT) is shown in Figure 2 (f-g) during both non-storm and storm time conditions. For non-storm conditions, the relationship is very similar to that of the overall trend for all MLT and appears to be dominated by the dawn-side behavior. It shows that substorm phase (identified by AE threshold) has little effect so that within 7 R_E, $\mathbf{J}_{\perp(\varphi)}$ is westward (reaching ~15 nA/m^2)**.** For storm times, however, the relationship is influenced by the local region around midnight, where in periods with no substorms, within 3.4 R_E $\mathbf{J}_{\perp(\varphi)}$ is westward (growing to ~8 nA/m^2), while between 3.4-7.5 R_E, $\mathbf{J}_{\perp(\varphi)}$ is westward (magnitude peak at ~15 nA/m^2). During substorm phases at these storm times, $\mathbf{J}_{\perp(\varphi)}$ is eastward within 3.2 R_E, while between 3.2-7 R_E, $\mathbf{J}_{\perp(\varphi)}$ is westward and suppressed in magnitude.

Figure 7 (h-i) panels explores the relationship between the MLT trends in $\mathbf{J}_{\perp(\varphi)}$ in a slightly different way by separating the behaviour (as a function of MLT) into ranges of L-shells at 2-4.8 R_E and 4.8-7 R_E. In the 2-4.8 R_E range, during quiet times, $\mathbf{J}_{\perp(\varphi)}$ is westward overall in the range 00:00-12:00 MLT and perhaps grows towards noon to a maximum of ~25 nA/m^2. In the region 05:00-07:00 MLT, $\mathbf{J}_{\perp(\varphi)}$ decreased significantly (to ~25 nA/m^2). From ~13:00 MLT $\mathbf{J}_{\perp(\varphi)}$ falls and turns eastward overall on the dusk side; so that from 12:00-19:00 MLT, $\mathbf{J}_{\perp(\varphi)}$ grows to a maximum eastward magnitude of about 40 nA/m^2. In the region 16:00-18:00 MLT, the current density decreases significantly. From 20:00-24:00 MLT, the median of $\mathbf{J}_{\perp(\varphi)}$ is unstable, consistent with the night-side, large error bars in panel (e). In the region 21:00-22:00 MLT, in particular, the current density is ~-25 nA/m^2. During storm conditions, this trend in $\mathbf{J}_{\perp(\varphi)}$ is similar to that of quiet time values, except that in the midnight region the median of $\mathbf{J}_{\perp(\varphi)}$ is stable and westward with magnitude of ~20 nA/m^2.

In the 4.8-7 R_E region, $\mathbf{J}_{\perp(\varphi)}$ is <15 nA/m^2 and always slightly eastward overall from 00:00-04:00 MLT (and also for 19:00-21:00 MLT). Elsewhere, $\mathbf{J}_{\perp(\varphi)}$ is westward and grows slightly to 10:00 MLT. From 15:00-18:00 MLT, the westward current grows to a maximum of >30 nA/m^2 (storm times). The magnitude decreases in the regions 10:00-14:00 and 16:00-18:00 MLT, but grows in the westward direction from 21:00-24:00 MLT. For both ranges of L, the westward current grows slowly towards noon, but the behaviour changes significantly from 15:00 MLT to the dusk-side, and from midnight to the dawn-side, where the maximum change is > 20 nA/m^2. This is consistent with indications from panels (b)-(e) and indeed the overall trends are consistent with those in the (m), (n) and (o) panels of Figure 1, confirming there is a split in the distribution at ~4.6-4.8 R_E on the dusk-side.

Finally, the (j) panel of Figure 7 shows the $\mathbf{J}_{\perp(R)}$ component at different MLTs. During quiet times, from 00:00-05:00 MLT J_R is outward, its magnitude grows to ~10 nA/m^2 at ~ 3:00 then decrease

gradually. It becomes earthward at ~05:30 MLT, < 5 nA/m^2. Briefly, however, its magnitude increases rapidly to ~20 nA/m^2 on the noon side then dips back to zero. At ~11:30 MLT, it becomes outward again with a small value of ~ 5 nA/m^2. From 12:30-24:00 MLT $\mathbf{J}_{\perp(R)}$ is earthward, < 5 nA/m^2. During storm times, the trend in $\mathbf{J}_{\perp(R)}$ is similar to quiet time values, except that from 20:00-23:00 MLT, $\mathbf{J}_{\perp(R)}$ is outward with a magnitude peak of ~10 nA/ m^2.

4 Discussion

We first note that these results show (for the average conditions of this year of data) the RC generally lies within 7.5 R_E, consistent with (Yang et al. 2016), with an inner eastward $\mathbf{J}_{\perp(\varphi)}$ and outer westward $\mathbf{J}_{\perp(\varphi)}$, reversing at ~3.2 R_E on the dawn-side, consistent with (Le, Russell, and Takahashi 2004). On the dusk-side, the eastward current widens, extending to ~3.6 R_E. During storm times, this eastward-westward boundary moves inwards on the dawn-side and noon-side, but moves outwards on the dusk-side (its full MLT form is not clear, since effects on the eastward current are suppressed at some MLT) and the westward current is enhanced for most MLTs. The median current density ranges from 15 nA/m^2 (quiet periods) to 20 nA/m^2 (storm-time). The inner, eastward current (mainly extending 09:00-18:00 MLT) is less clear in the midnight sector. During storm conditions, the westward current outside 4.5 R_E is present for almost all MLTs, but it is suppressed on the dusk-side. We suggest three key effects:

1. A westward current dawn-dusk asymmetry which is dominant on the dawn-side (to noon) and is possibly linked to FAC connectivity (as suggested by Zhang et al. (2011)); but here the distribution has been shown in detail with radial distance.

2. An asymmetric (partial) inner eastward current, which widens into a banana-like current on the noon side (10:00-16:00 MLT), broadly suggestive of the scenario of Liemohn et al. (2013); see discussion below.

3. A sharp inner boundary (~3.2 R_E) within which a persistent eastward current exists. The position of these boundaries is affected by geomagnetic activity.

Secondly, we note that, although this morphology reflects the direct estimate of current density from curl B, the RC density from formula (2) depends on the perpendicular pressure grad and the anisotropy of plasma. It is difficult physically to absolutely satisfy the isotropic pressure condition in the RC region, especially during non-storm periods, and indeed the plasma moment data can have significant errors. Based on the RBSP observational total pressure and $P_\perp/P_\parallel$ (from Figure 1 of (Yue et al. 2019), and the dipole field hypothesis, there is a rough contribution of the anisotropy term of formula (2) to the RC in terms of L and for different phases during geomagnetic storms. This is shown in Figure 9, which indicates that the anisotropy contributes an eastward $\mathbf{J}_\varphi$ and plays an insignificant role for the main RC. If this anisotropy term is ignored, J mainly relates to pressure gradient (first term on equation 2) and Liemohn et al. (2013) pointed out that a pressure peak can produce a closed banana-like current from grad P: inside the peak, $\boldsymbol{J}$ is eastward, while outside, $\boldsymbol{J}$ is westward. In our results, the combined noon regions (10:00-16:00 MLT) have similar characteristics, suggesting a pressure peak (near 4.8 R_E and dusk) is present, and thus closing the banana current.

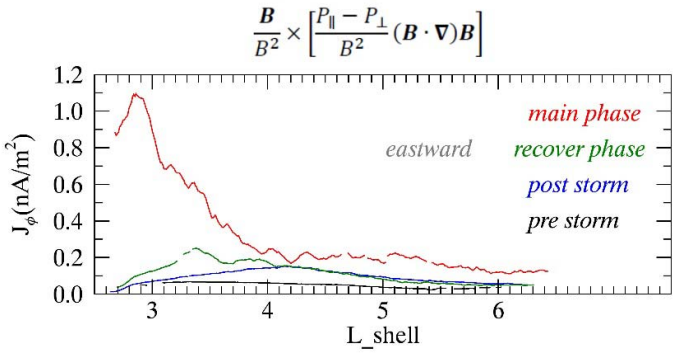

Figure 9. The dependence of the current density from the anisotropy term of formula (2) on main and recovery phases and post and pre-storm. Total pressure and pressure anisotropy data are from Figure 1 of (Yue et al. 2019).

Conversely, if there is a valley in plasma pressure, formula (2) suggests a closed banana current will also be produced: inside the valley, $\boldsymbol{J}$ will be westward, while outside $\boldsymbol{J}$ will be eastward. The night side, post-midnight (00:00-06:00 MLT) shows this feature. Thus, a corresponding pressure valley exists in this region and results in a reverse closure banana current. For magnetically quiet time, the pressure valley is around 4.8 R_E; moving toward the magnetotail (midnight) during storms his behaviour is confirmed in Figure 7 (f-g)), i.e. during non-storm times, substorms inject particles into the region outside the pressure valley (increasing the pressure gradient) and the westward current outside the valley increases significantly; while during storm periods, substorm onsets may inject particles into the valley (reducing gradients).

These two banana-like currents (the noon side and post-midnight) can also be seen in Figure 10. These three panels are defined as for Figure 6, except that we use medians here instead of means (to better compare with the trends in Figure 7). Clearly, these distributions demonstrate the key statistical differences which predominantly affect the dusk side from noon. We suggest two reasons for the overall observed behaviour and difference in the plots:

1. Due to limited data limitations, we only use a relatively simple classification standard of geomagnetic conditions. The use of median statistics will exclude some values with large deviations, which may correspond to true values under other abnormal magnetic conditions.

2. The plasma distribution on the noon side does not maintain a large, outer pressure gradient but the inner eastward current always exists because the inner magnetic field can more easily maintain a balance with a big pressure gradient.

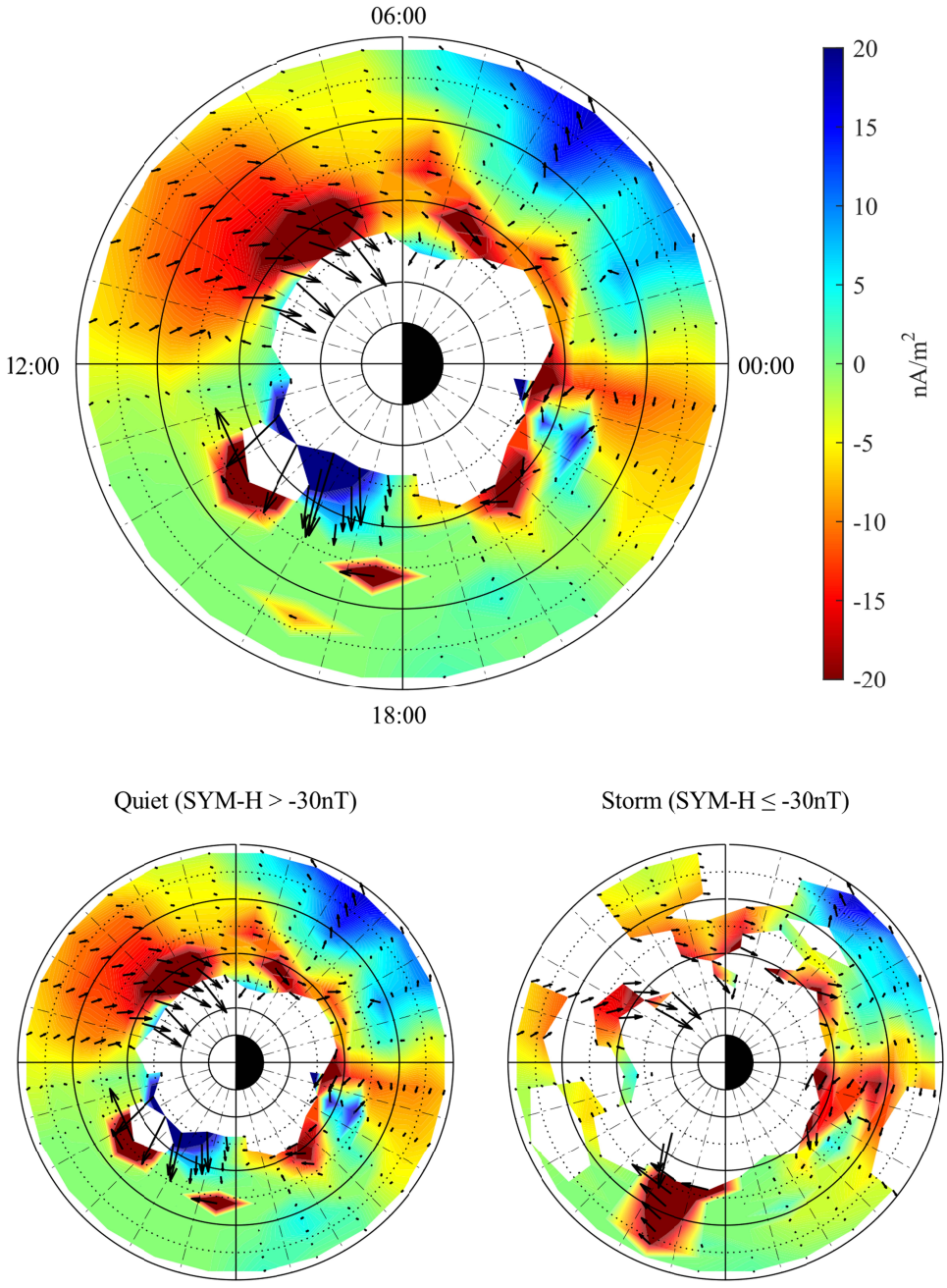

Figure 10. Contour of $\mathbf{J}_{\perp(\varphi)}$ distribution for medians under all magnetic conditions (upper panel) and during non-storm/storm period (lower panels).

For the two most obvious banana currents (one is inner eastward/outer westward and centered at the noon side and the other one is inner westward/outer eastward and centered at ~03:00MLT), we can consider the suggestions of (Yue et al. 2018) who showed statistical pressure distribution plots (their Figure 2, left hand) demonstrating that different species of particles may contribute to different regions. In their plots, several peaks of total pressure lie in the region ~3-4 R_E from 12:00 to 01:00 MLT and Yue et al. conclude there are two clear boundaries at 12:00MLT and 01:00MLT. A key

difference to the results here is that Yue et al show an obvious valley at 01:00MLT, which they attribute to contributions of oxygen pressure and electron pressure. The two banana-like currents that we have discussed above, however, can't be directly supported by the pressure values in (Yue et al. 2018). Perez et al. (2015) observed multiple peaks in the ion flux of trapped particles in the RC region by TWINS ENA stereoscopic imaging. Here again, we can see that a valley formed by two peaks exits in the region ~5-6 R_E from 00:00 to 03:00 MLT.

It is therefore not unlikely that the smaller scale structures, seen here directly from the magnetic field data, do exist. In fact, previous studies have shown that the occurrence of multiple plasma pressure peaks in the RC region are common, but also transient. Actually, the RC morphology shown here is a combination of different times and the time-range of data used is just a little more than one year and may not be wholly representative of the average distribution of the RC for very long time periods. This difference is clearly shown between two panels of Figure 11. Average distribution of longer time range shows more order.

A third feature to consider is that there is an obvious earthward deflection of the inner current directions at the dawn-noon side and an anti-earthward deflection at the noon-dusk side, as seen in the radial components of the arrows in Figures 6 and10. We suggest the reason is the boundary of a plasma peak always exits at the noon-side. The gradient of pressure makes outside current flow clockwise. Thus, it should be earthward here. This earthward deflection and the inner eastward current are also clearly shown in the left-hand panel of Figure 11, which illustrates the statistical, perpendicular current distribution from Cluster data. It should be noted that whole Cluster data set is taken during a much wider range of geomagnetic conditions and Cluster only accessed the inner current (< 4 R_E) for small part of the later mission. It therefore missed much of the dusk-noon side inner signatures. Nevertheless, it shows similar morphology to MMS and the earthward deflection is seen on the dawn side. The right-hand panel of Figure 11 shows that Cluster sees a similar form for the outer RC as MMS during the same epoch.

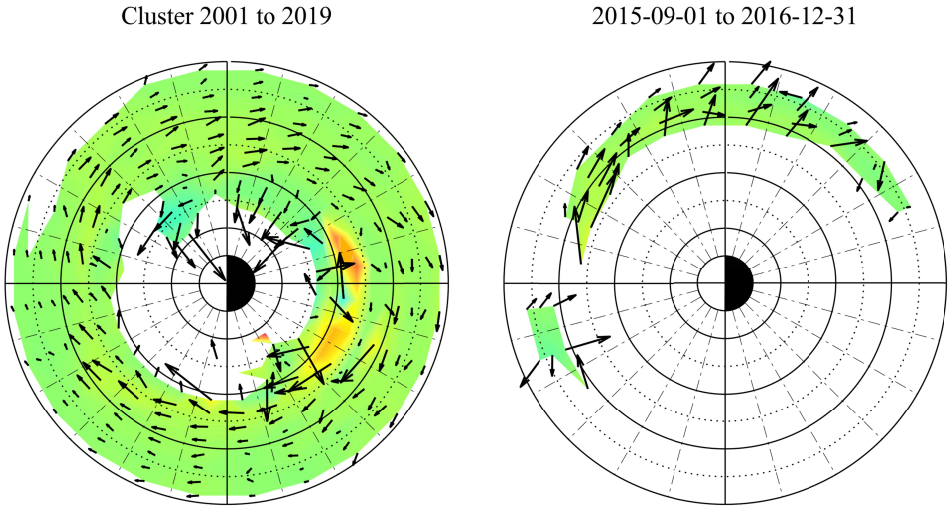

Figure 11. Statistical results from 19 years of Cluster FGM data (2001-2019), represented as before on the same near equatorial, SM grid as Figures 6 and 10 (noon on the left). The valid data time range of the right panel is the same as for the MMS data we analyze in this paper. The colour bars of these figures are the same as Figure 10.

A fourth issue is that clearly our results cannot support the theory of a dominant dusk side partial RC. There is no obvious enhancement of the westward current on the dusk-side during storm periods, although we suggested in section 3 that this may be due to both a widening of the outer RC region, rather than a local increase in current density, and the strong asymmetry in the eastward current. Here the westward current on the dawn-side plays a dominant role both during non-storm period and storm periods. The RC morphology is much more complex than the image of a symmetric RC + an asymmetric RC. Indeed, Zhang et al. 2011 suggested that the enhancement of the dawn side current from noon and suppression of growth on the dusk side could reflect the role of the connecting Region 2 field-aligned currents, which are upward on the dawn side (enhancing the dawn side RC) and downward on the dusk side (depleting the dusk side RC). This last point is an issue we will investigate in future work using low orbit data in combination with MMS.

The last points we note here are that the outer westward current around noon seems to show a dip, both in Figure 6 and Figure 10, but it is smoothly continuous in Figure 11. We expect this is due to the wider range of geomagnetic conditions covered by Cluster. In fact, the right panel of Figure 11 doesn't show the outer eastward current of a counter-clockwise banana current, although it indeed shows some outward deflection. Overall, the magnitude of current density in Figure 11 is smaller than that in Figure 6/10, as noted in section 3. As we suggested, this is because the smaller spatial scale of MMS captures the fine structures (typically intense small-scale currents) which contribute to the current densities. Since we limit the magnetic latitude of the tetrahedral barycenter in a narrow slot ($\pm 20°$) near the equatorial plane, Cluster, with a more inclined orbit for most of the mission (and outer perigee), and because of its much larger tetrahedron configuration, tends to sample positions further out than MMS. Thus, we expect that smaller current densities will be obtained from Cluster if the RC contains localized mesoscale structures.

The difference between MMS and Cluster results and the discontinuity of the westward current near noon shown in Figure 6/10 also suggest the existence of a current structure smaller than the entire RC scale. These structures are not fully displayed due to the limitations of the area of focus in this paper. We have attached a picture of the MMS current distribution at higher latitudes to the supplementary material (S1). It suggests westward current on the noon side complete closure at higher latitudes. The relevant analysis is in progress, which will be the beginning of the discussion in our next paper.

5 Summary

Using the curlometer, we have calculated $\boldsymbol{J}$ with one-minute cadence to directly show the form of the eastward-westward current reversal and current asymmetry, both in a typical case study and statistically. We extract the morphology of $\mathbf{J}_\varphi$, and its distribution characteristics, in MLT and radial distance (L-shell) from the statistical distribution.

Firstly, we broadly confirm previous results that the RC lies mainly within 7.5 R_E with an inner eastward current and a westward outer current (Le, Russell, and Takahashi 2004; Yang et al. 2016). During non-storm time, the dawn-side westward current is significantly larger than on the dusk side (Zhang et al. 2011). The high spatial resolution from MMS, and a more complete RC coverage, however, reveals new features in both MLT and L-shell. Indeed, a comparison with the later dataset of Cluster (as well as the interval overlapping with MMS) shows that these results remain consistent within the sampling constraints of each mission.

Secondly, the detailed form of the eastward current, radially and as a function of MLT, is shown in

terms of its competing effect with the westward current, for the first time. We deduce there is a closed banana current due to a peak in plasma pressure at ~4.8 R_E on the afternoon side (evolving into a more complex form across noon). The morphology suggested by Liemohn et al. (2013) is extended by proposing an additional banana current due to a night-side valley of plasma pressure at ~4.8 R_E. There is limited data from the plasma instrument onboard MMS while in the RC, limiting direct observational evidence of the pressure gradients. Nevertheless, we suggest these two banana currents exist in both magnetically quiet and storm-time periods. During storms, the center of the banana current center moves (earthwards on the dayside and outwards on the night-side). The main enhanced morphology is that the banana current density caused by the pressure peak increases, while the banana current density caused by the valley of pressure will decrease.

Thirdly, the overall enhancement of the RC at the dusk-side during storm period is insignificant. This can't provide an evidence support for the partial RC theory; but does support banana like currents in the pre-terminator, dusk-side region and post terminator dawn-side region. In future work we are investigating the connectivity of the R2 FACs which may play a role in mitigating the effects of the dawn-side and dusk-side current densities (as discussed above), depending on the nature of the current closure either through the banana currents or via the ionosphere. These effects are likely to depend on the geomagnetic activity levels. There is also some indication that the local current density does not show a strong enhancement because the dusk-side current widens in radial range giving an increase in total current.

Acknowledgments

This work was supported by the NSFC grants 41821003 and 41874193; Natural Environment Research Council (NERC) Highlight Topic SWIGS grant NE/P016863/1; and STFC in-house research grant ST/M001083/1.

Open Research

Datasets for this research are available in these following sources: OMNI data https://spdf.gsfc.nasa.gov/pub/data/omni/omni_cdaweb/hro_1min/; MMS FGM data https://spdf.gsfc.nasa.gov/pub/data/mms/; Our calculated results of current density https://doi.org/10.5281/zenodo.5574704.

References

Chen, Y. Q., M. Wu, T. L. Zhang, Y. Huang, G. Q. Wang, R. Nakamura, W. Baumjohann, C. T. Russell, B. J. Giles, and J. L. Burch. 2021. 'Statistical Characteristics of Field Aligned Currents in the Plasma Sheet Boundary Layer', *Journal of Geophysical Research (Space Physics)*, 126: e28319.

Daglis, Ioannis A., Richard M. Thorne, Wolfgang Baumjohann, and Stefano Orsini. 1999. 'The terrestrial ring current: Origin, formation, and decay', *REVIEWS OF GEOPHYSICS*, 37: 407-38.

Dong, X. C., M. W. Dunlop, T. Y. Wang, J. B. Cao, K. J. Trattner, R. Bamford, C. T. Russell, R. Bingham, R. J. Strangeway, R. C. Fear, B. L. Giles, and R. B. Torbert. 2018. 'Carriers and Sources of Magnetopause Current: MMS Case Study', *Journal of Geophysical Research: Space Physics*, 123: 5464-75.

Dunlop, M. W. 2002. 'Four-point Cluster application of magnetic field analysis tools: The Curlometer', *Journal of Geophysical Research*, 107.

Dunlop, M. W., X. -C. Dong, T. -Y. Wang, J. P. Eastwood, P. Robert, S. Haaland, Y. -Y. Yang, P. Escoubet, Z. -J. Rong,

C. Shen, H. -S. Fu, and J. De Keyser. 2021. 'Curlometer Technique and Applications', *Journal of Geophysical Research (Space Physics)*, 126: e29538.

Dunlop, M. W., S. Haaland, X. C. Dong, H. R. Middleton, C. P. Escoubet, Y. Y. Yang, Q. H. Zhang, J. K. Shi, and C. T. Russell. 2018. 'Multipoint Analysis of Electric Currents in Geospace Using the Curlometer Technique.' in, *Electric Currents in Geospace and Beyond*.

Dunlop, M. W., D. J. Southwood, K. -H. Glassmeier, and F. M. Neubauer. 1988. 'Analysis of multipoint magnetometer data', *Advances in Space Research*, 8: 273.

Jorgensen, A. M. 2004. 'A statistical study of the global structure of the ring current', *Journal of Geophysical Research*, 109.

Le, G., and C. T. Russell. 1998. 'Initial Polar magnetic field experiment observations of the low-altitude polar magnetosphere: Monitoring the ring current with polar orbiting spacecraft', *Journal of Geophysical Research: Space Physics*, 103: 17345-50.

Le, G., C. T. Russell, and K. Takahashi. 2004. 'Morphology of the ring current derived from magnetic field observations', *Annales Geophysicae*, 2004: 29.

Le, Guan, William J. Burke, Robert F. Pfaff, Henry Freudenreich, Stefan Maus, and Hermann Lühr. 2011. 'C/NOFS measurements of magnetic perturbations in the low-latitude ionosphere during magnetic storms', *Journal of Geophysical Research: Space Physics*, 116.

Liemohn, Michael W., Natalia Yu Ganushkina, Roxanne M. Katus, Darren L. De Zeeuw, and Daniel T. Welling. 2013. 'The magnetospheric banana current', *Journal of Geophysical Research: Space Physics*, 118: 1009-21.

Parker, E. N. 1957. 'Newtonian Development of the Dynamical Properties of Ionized Gases of Low Density', *Physical Review*, 107: 924-33.

Paschmann, G., and S. J. Schwartz. 1998. "ISSI Book on Analysis Methods for Multi-Spacecraft Data." In, 99.

Perez, J. D., J. Goldstein, D. J. McComas, P. Valek, N. Buzulukova, M. -C. Fok, and H. J. Singer. 2015. 'TWINS stereoscopic imaging of multiple peaks in the ring current', *Journal of Geophysical Research (Space Physics)*, 120: 368.

Robert, Patrick, Alain Roux, Christopher C. Harvey, Malcolm W. Dunlop, Patrick W. Daly, and Karl-Heinz Glassmeier. 1998. 'Tetrahedron Geometric Factors', *ISSI Scientific Reports Series*, 1: 323.

Russell, C. T. 1971. 'Geophysical coordinate transformations', *Cosmic Electrodynamics*, 2: 184.

Russell, C. T., B. J. Anderson, W. Baumjohann, K. R. Bromund, D. Dearborn, D. Fischer, G. Le, H. K. Leinweber, D. Leneman, W. Magnes, J. D. Means, M. B. Moldwin, R. Nakamura, D. Pierce, F. Plaschke, K. M. Rowe, J. A. Slavin, R. J. Strangeway, R. Torbert, C. Hagen, I. Jernej, A. Valavanoglou, and I. Richter. 2014. 'The Magnetospheric Multiscale Magnetometers', *Space Science Reviews*, 199: 189-256.

Shen, C., Y. Y. Yang, Z. J. Rong, X. Li, M. Dunlop, C. M. Carr, Z. X. Liu, D. N. Baker, Z. Q. Chen, Y. Ji, and G. Zeng. 2014. 'Direct calculation of the ring current distribution and magnetic structure seen by Cluster during geomagnetic storms', *Journal of Geophysical Research :Space Physics*, 119: 2458.

Sitnov, M. I., G. K. Stephens, N. A. Tsyganenko, H. Korth, E. C. Roelof, P. C. Brandt, V. G. Merkin, and A. Y. Ukhorskiy. 2020. 'Reconstruction of Extreme Geomagnetic Storms: Breaking the Data Paucity Curse', *Space Weather*, 18: e02561.

Stephens, G. K., S. T. Bingham, M. I. Sitnov, M. Gkioulidou, V. G. Merkin, H. Korth, N. A. Tsyganenko, and A. Y. Ukhorskiy. 2020. 'Storm Time Plasma Pressure Inferred From Multimission Measurements and Its Validation Using Van Allen Probes Particle Data', *Space Weather*, 18: e02583.

Stephens, G. K., M. I. Sitnov, A. Y. Ukhorskiy, E. C. Roelof, N. A. Tsyganenko, and G. Le. 2016. 'Empirical modeling of the storm time innermost magnetosphere using Van Allen Probes and THEMIS data: Eastward and banana currents', *Journal of Geophysical Research (Space Physics)*, 121: 157-70.

Thébault, Erwan, Christopher C. Finlay, Ciarán D. Beggan, Patrick Alken, Julien Aubert, Olivier Barrois, Francois

Bertrand, Tatiana Bondar, Axel Boness, Laura Brocco, Elisabeth Canet, Aude Chambodut, Arnaud Chulliat, Pierdavide Coïsson, François Civet, Aimin Du, Alexandre Fournier, Isabelle Fratter, Nicolas Gillet, Brian Hamilton, Mohamed Hamoudi, Gauthier Hulot, Thomas Jager, Monika Korte, Weijia Kuang, Xavier Lalanne, Benoit Langlais, Jean-Michel Léger, Vincent Lesur, Frank J. Lowes, Susan Macmillan, Mioara Mandea, Chandrasekharan Manoj, Stefan Maus, Nils Olsen, Valeriy Petrov, Victoria Ridley, Martin Rother, Terence J. Sabaka, Diana Saturnino, Reyko Schachtschneider, Olivier Sirol, Andrew Tangborn, Alan Thomson, Lars Tøffner-Clausen, Pierre Vigneron, Ingo Wardinski, and Tatiana Zvereva. 2015. 'International Geomagnetic Reference Field: the 12th generation', *Earth, Planets and Space*, 67.

Tsyganenko, N. A., V. A. Andreeva, M. I. Sitnov, G. K. Stephens, J. W. Gjerloev, X. Chu, and O. A. Troshichev. 2021. 'Reconstructing Substorms via Historical Data Mining: Is It Really Feasible?', *Journal of Geophysical Research (Space Physics)*, 126: e29604.

Vallat, C., I. Dandouras, and M. Dunlop. 2005. 'First current density measurements in the ring current region using simultaneous multi-spacecraft CLUSTER-FGM data', *Annales Geophysicae*, 2005.

Yang, Y. Y., C. Shen, M. Dunlop, Z. J. Rong, X. Li, V. Angelopoulos, Z. Q. Chen, G. Q. Yan, and Y. Ji. 2016. 'Storm time current distribution in the inner equatorial magnetosphere: THEMIS observations', *Journal of Geophysical Research: Space Physics*, 121: 5250-59.

Yue, Chao, Jacob Bortnik, Wen Li, Qianli Ma, Matina Gkioulidou, Geoffrey D. Reeves, Chih-Ping Wang, Richard M. Thorne, Anthony T. Y. Lui, Andrew J. Gerrard, Harlan E. Spence, and Donald G. Mitchell. 2018. 'The Composition of Plasma inside Geostationary Orbit Based on Van Allen Probes Observations', *Journal of Geophysical Research (Space Physics)*, 123: 6478-93.

Yue, Chao, Jacob Bortnik, Wen Li, Qianli Ma, Chih-Ping Wang, Richard M. Thorne, Larry Lyons, Geoffrey D. Reeves, Harlan E. Spence, Andrew J. Gerrard, Matina Gkioulidou, and Donald G. Mitchell. 2019. 'Oxygen Ion Dynamics in the Earth's Ring Current: Van Allen Probes Observations', *Journal of Geophysical Research: Space Physics*, 124: 7786-98.

Zhang, Q. H., M. W. Dunlop, M. Lockwood, R. Holme, Y. Kamide, W. Baumjohann, R. Y. Liu, H. G. Yang, E. E. Woodfield, H. Q. Hu, B. C. Zhang, and S. L. Liu. 2011. 'The distribution of the ring current: Cluster observations', *Annales Geophysicae*, 29: 1655-62.